Acta Oceanol. Sin., 2021, Vol. 40, No. 5, P. 105–113
https://doi.org/10.1007/s13131-020-1681-2
http://www.hyxb.org.cn
E-mail: ocean2@hyxb.org.cn

Distal axis sulfide mineralization on the ultraslow-spreading Southwest Indian Ridge: an LA-ICP-MS study of pyrite from the East Longjing-2 hydrothermal field

Shili Liao[1, 2], Chuanwei Zhu[3], Jianping Zhou[1, 2], Weiyong Liu[1, 2], Junyu Yu[1, 2], Jin Liang[1, 2], Weifang Yang[1, 2], Wei Li[1, 2], Jia Liu[4], Chunhui Tao[1, 2]*

[1] Second Institute of Oceanography, Ministry of Natural Resources, Hangzhou 310012, China

[2] Key Laboratory of Submarine Geosciences, Ministry of Natural Resources, Hangzhou 310012, China

[3] State Key Laboratory of Ore Deposit Geochemistry, Institute of Geochemistry, Chinese Academy of Sciences, Guiyang 550081, China

[4] Key Laboratory of Geoscience Big Data and Deep Resource of Zhejiang Province, School of Earth Sciences, Zhejiang University, Hangzhou 310027, China

Received 14 March 2020; accepted 13 July 2020

Abstract

The newly discovered East Longjing-2 hydrothermal field (ELHF-2) is located on the Dragon Horn oceanic core complex of the ultraslow-spreading Southwest Indian Ridge, approximately 12 km from the ridge axis. This study measured the chemical compositions of pyrite from ELHF-2 using a laser ablation inductively coupled plasma mass spectrometry (LA-ICP-MS) to investigate the genesis of the field. Three generations of pyrite were classified, and found that: Py1 and Py2, rich in V, Mn, U, and Se, occur in altered basalt debris and the silica alteration matrix, respectively. Py3 was mainly intergrown with chalcopyrite in quartz veins and had higher Cu, In, Ag, Sb, and Au contents than Py1 and Py2. Some elements, such as Au, Se, and Pb, are likely presented as direct substitution with Fe^{2+} in pyrite, while Cu, Zn, Co, Ni, and Ag probably occur both as direct substitution with Fe and as distributed micro- to nanoparticle-sized sulfides. Meanwhile, the occurrence of V, Mn, and U is likely presented as oxide inclusions. Trace element geochemistry suggested that the pyrite was formed under high-temperature conditions, and the ore forming elements were likely derived from ultramafic rocks. In addition, Py1 and Py2 were formed under higher water/rock ratio and higher temperature conditions, with more seawater involvement compared with Py3. The formation of ELHF-2 was probably driven by exothermic serpentinization reactions with an additional magmatic heat. This study shows that high-temperature hydrothermal circulation driven by magmatic activity can be developed on distal rift flank areas of magma-starved ultraslow-spreading ridges.

Key words: pyrite geochemistry, LA-ICP-MS, hydrothermal activity, Southwest Indian Ridge

Citation: Liao Shili, Zhu Chuanwei, Zhou Jianping, Liu Weiyong, Yu Junyu, Liang Jin, Yang Weifang, Li Wei, Liu Jia, Tao Chunhui. 2021. Distal axis sulfide mineralization on the ultraslow-spreading Southwest Indian Ridge: an LA-ICP-MS study of pyrite from the East Longjing-2 hydrothermal field. Acta Oceanologica Sinica, 40(5): 105–113, doi: 10.1007/s13131-020-1681-2

1 Introduction

Since hydrothermal activity was first observed on the Galapagos Rift (Corliss et al., 1979), huge progress has been made in determining the genesis and ore-forming processes of sulfides on mid-ocean ridges (MORs) by studying sulfide chimneys and the surface products of hydrothermal activities (Fouquet et al., 2010; Hannington et al., 2005; Haymon, 1983; Marques et al., 2011; Murton et al., 2019). Numerous studies have demonstrated that there are mainly two types of hydrothermal activities on MORs (Fouquet et al., 2010; German et al., 2016): (1) magma-controlled hydrothermal fields (HFs), which developed on all types of MORs, and (2) tectonically controlled HFs, that mainly developed on slow and ultraslow spreading ridges and may constitute 50% of the total HFs that occur on the slow-spreading Mid-Atlantic Ridge (German et al., 2016). Tectonically controlled HFs exhibit diverse features (e.g., high-temperature sulfide sites, low-temperature carbonate sites, and diffuse flows; Bemis et al., 2012), and the heat source for these systems has often been directly linked to either the exothermic reaction of serpentinization with or without an additional magmatic heat (German et al., 2016).

The ultraslow-spreading Southwest Indian Ridge (SWIR) was considered as a desert of hydrothermal activities. Since the first active HF (Longqi-1) was discovered (Tao et al., 2012), further abundant hydrothermal activities have been revealed, such as the Duanqiao-1, Yuhuang-1, Changbai-1, Tiancheng-1, Tianzuo-1, and Suye fields (Tao et al., 2014). These HFs are distributed across diverse geological settings and exhibit different mineraliz-

---

Foundation item: The National Key Research and Development Program of China under contract Nos 2016YFC1401210, 2018YFC0309902 and 2017YFC0306603; Zhejiang Provincial Natural Science Foundation of China under contract No. LQ19D060002; the National Natural Science Foundation of China under contract No. 42006074; China Ocean Mineral Resources R&D Association Project under contract No. DY135-S1-1-02.

*Corresponding author, E-mail: taochunhuimail@163.com, taochunhui@sio.org.cn ation features (Chen et al., 2018; Liao et al., 2018; Tao et al., 2011; Yang et al., 2016; Ye et al., 2012). The newly discovered East Longjing-2 hydrothermal field (ELHF-2) is among the currently discovered HFs that are furthest away from the ridge axis (12 km) on ultraslow-spreading ridges. Hydrothermal systems cannot directly mine heat from a ridge axis at such a distance. Understanding the genesis of this field is critical to understand the factors controlling hydrothermal activity development on distal ultraslow spreading ridge flanks.

Pyrite is a universal mineral that forms under wide conditions during the mineralization process (Keith et al., 2016a). It contains a wide range of trace elements (e.g., Cu, Pb, Zn, Ag, As, Sb, Co, Ni, Se, Te, and Hg), in the form of Fe/S substitution in crystal lattice or as micro- to nanoparticle-sized mineral inclusions (Keith et al., 2016b; Reich et al., 2013). The trace element enrichment features and their occurrences in pyrite not only provide information about mineral/fluid partitioning of metals, but also constrain the evolution of physicochemical conditions during the mineralization process (Reich et al., 2013; Zhang et al., 2014; Zhao et al., 2011). Here, the mineralogy and pyrite chemistry of sulfide-rich samples collected from ELHF-2 were analyzed to reveal its genesis and improve the knowledge of hydrothermal systems developed on ultraslow-spreading ridges.

2 Geological background

The study area, located between the Indomed and Gallieni transform faults of the ultraslow-spreading SWIR (Fig. 1a). This segment of the ridge has a semi-spreading rate of about 0.7–0.9 cm/a (Dick et al., 2003). This section of the ridge is characterized by highly asymmetric topography cut by a series of large, long-term, active NS-striking transform faults. Because of the Marion and Crozet hotspots, the 49°–52°E ridge section shows strong negative residual mantle Bouguer gravity anomalies, indicating relatively active crust–mantle exchange, deep magmatism, and sufficient magma supply (Georgen et al., 2001; Li et al., 2015; Sauter et al., 2009). Previous investigations have reported intensive hydrothermal activity with a frequency of about 2.5 sites per 100 km (Tao et al., 2012, 2014), the control of which has been attributed to enhanced local magma supply and suitable crustal permeability (Tao et al., 2012).

ELHF-2 (37.85°S, 49.80°E), located about 12 km away from the ridge axis on the southern rift flank of the segments 28 at a water depth of about 1 780 m. This field, discovered in 2016 during the 40th cruise, is located on the Dragon Horn oceanic core complex (OCC) that composed by a twin detachment fault system (Tao et al., 2020). ELHF-2 is developed adjacent to the dome-shaped detachment surface formed by the more mature first-stage detachment fault (DF1) (Fig. 1b). In the north of this field, two additional HFs, the Longqi-1 and Suye (so called Longqi-3) fields, form a possibly linear mineralized zone along the active second-stage detachment fault (DF2) (Tao et al., 2020). Most of this field is exposed as surface sediments. The collected wall rocks were strongly chloritized and interpenetrated by minor sulfide-bearing quartz veins. The collected sulfide-rich samples were comprised mainly of disseminated mineralized ores, and no evidence of fluid venting was observed, suggesting that this field is inactive.

3 Mineralogy

The samples were collected during the 2015–2016 DY125-40 cruise on R/V *Xiangyanghong 10*. Only one station of sulfide-rich samples was collected using a TV-grab, being intensively chlorit-

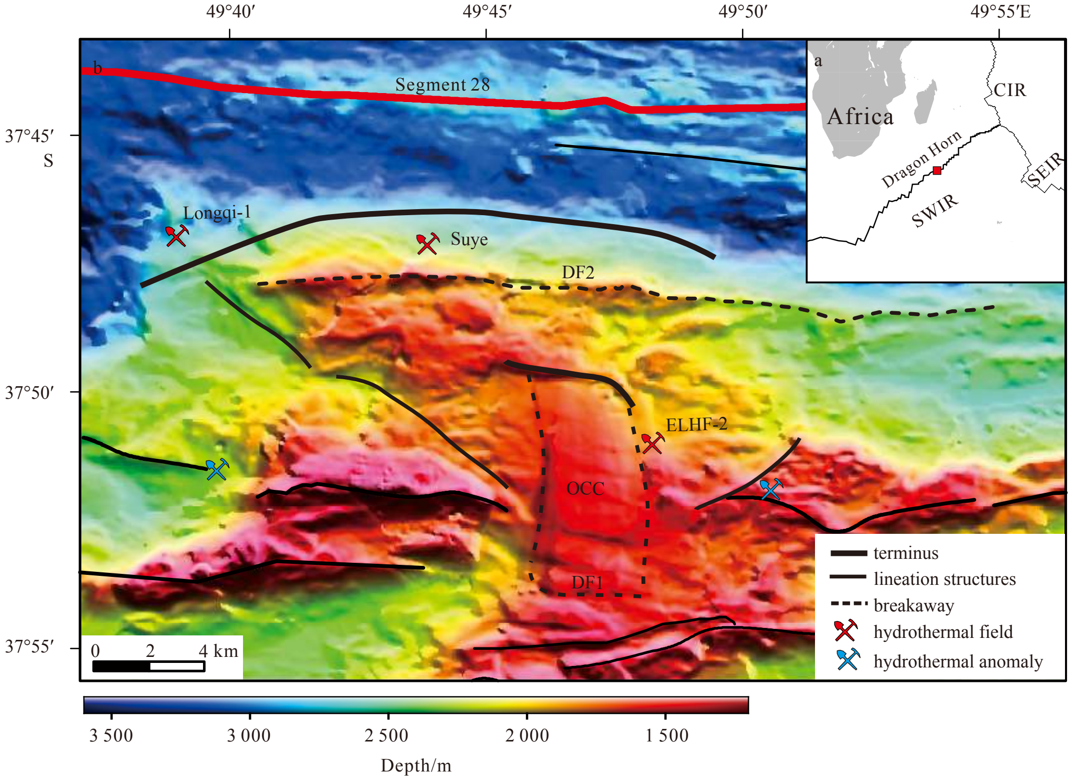

Fig. 1. Location of East Longjing-2 hydrothermal field (ELHF-2). The distribution of structures is according to Tao et al. (2020). Topography data for b were obtained by multibeam bathymetry survey. OCC: oceanic core complex, DF1: first-stage detachment fault, DF2: second-stage detachment fault, SWIR: Southwest Indian Ridge, SEIR: Southeast Indian Ridge, CIR: Central Indian Ridge.

ized and silicified basalt. The sulfide occurred as veinlets cutting the basal. Microscopic observation suggested that the main minerals are pyrite and chalcopyrite with minor limonite (Fig. 2). The gangue minerals are mainly quartz.

Three generations of pyrite were observed. The first generation, Py1 (euhedral to anhedral pyrite exhibiting residual corrosion features), was distributed in the altered basalt debris that was cemented by a silicon matrix and was partially or totally oxidized to limonite (Figs 2a and b). The second generation, Py2 (anhedral to euhedral), was mainly developed in the silicified alteration matrix (Fig. 2c). The third generation, Py3, was mainly distributed and coexisting with chalcopyrite in quartz veins that cross-cutting both the silica alteration matrix and the altered basalt debris (Figs 2d and e).

There were two generations of chalcopyrite. The first generation, Ccp1, with covellite rims, was distributed in the silica alteration matrix (Fig. 2f). However, it was not found to be in contact with Py2. The second generation, Ccp2, was mainly distributed in a late-stage quartz vein and coexisted with Py3 (Figs 2d and e).

4 Methods

Trace element concentrations of pyrite from ELHF-2 were analyzed by a laser ablation inductively coupled plasma mass spectrometry (LA-ICP-MS) at the State Key Laboratory of Ore Deposit Geochemistry, Institute of Geochemistry, Chinese Academy of Sciences. A 193 nm excimer laser system (RESOLution-LR-S155, Australian Scientific Instruments Pty Ltd., Australia) was employed as a laser sampler with an ICP-MS instrument (7700x, Agilent Technologies Inc., American) for the acquisition of ion-signal intensities. Ar gas was used as the transport gas, with a gas flow rate at 900 mL/min. Data were collected for 60 s after the signal intensity stabilized (generally after 30 s). The pit size, pulse frequency, and fluence were 26 μm, 5 Hz, and 3 J/cm^2, respectively. Peru Py, an internal laboratory standard, was used to calibrate the contents of the S and Fe; GSE-1G and GSD-1G were used to calibrate the contents of the lithophile elements; and STDGL3 was used to calibrate the contents of the chalcophile and siderophile elements (Danyushevsky et al., 2011). A sulfide reference material (MASS-1) was analyzed to monitor the data quality during the MS measurements.

5 Results

The pyrite in the samples was characterized by high Co, Ni, Cu, Zn, As, and Pb contents (Table 1). Py1 and Py2 exhibited comparable trace element enrichment features, with higher contents of V, Mn, U, and Se compared with Py3, ranging between 20.9×10^{-6}–98.8×10^{-6} (average 57.5×10^{-6}), 36.5×10^{-6}–332.8×10^{-6} (average 141.8×10^{-6}), 0.2×10^{-6}–0.6×10^{-6} (average 0.3×10^{-6}), 9.3×10^{-6}–38.9×10^{-6} (average 22.4×10^{-6}) and 4.2×10^{-6}–119.2×10^{-6} (average 43.4×10^{-6}), 13.7×10^{-6}–310.4×10^{-6} (average 119.0×10^{-6}), and 0.2×10^{-6}–3.0×10^{-6} (average 0.7×10^{-6}), 9.2×10^{-6}–97.5×10^{-6} (average 28.2×10^{-6}), respectively. Py3 contained higher amounts of Cu, In, Ag, Sb, and Au compared with the earlier stage pyrites, ranging between 446.3×10^{-6}–$6\,541.7\times10^{-6}$ (average $2\,985.0\times10^{-6}$), 0.4×10^{-6}–55.2×10^{-6} (average 11.6×10^{-6}), 1.3×10^{-6}–18.8×10^{-6} (average 6.1×10^{-6}), 0.2×10^{-6}–$5.\ 9\times10^{-6}$ (average 1.5×10^{-6}), and 0.1×10^{-6}–1.5×10^{-6} (average 0.6×10^{-6}), respectively.

6 Discussion

6.1 *Trace metal speciation in pyrite*

Numerous studies have shown that the trace elements found in pyrite mainly occur in three forms: as the substitution of Fe in the pyrite crystal lattice, as micro- to nanoparticle-sized sulfides, and as micro- to nano-sized oxide minerals or sulfates (Keith et al., 2016a; Meng et al., 2020). In the pyrite from ELHF-2, the enrichment of V, Co, Ni, Mn, Cu, Zn, As, Pb, and Se was apparent (Fig. 3). Because the pyrite crystals in this study were mostly eu-

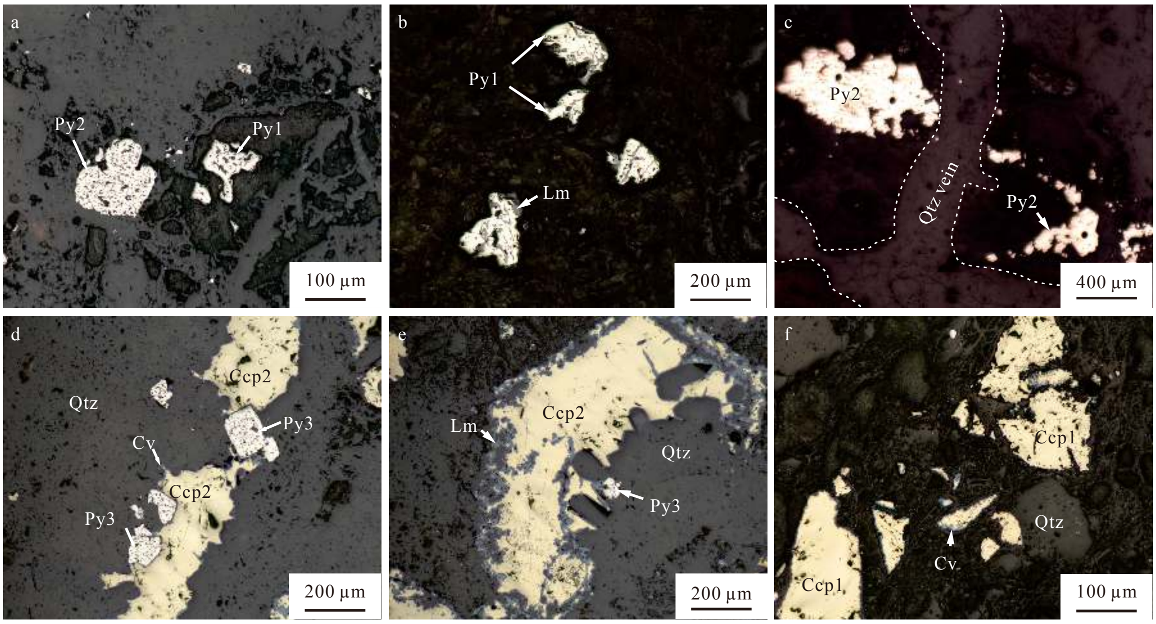

Fig. 2. Microscope photos of sulfide from ELHF-2. a. Py1 in altered basalt debris cemented by Py2-bearing silica matrix; b. Py1 in altered basalt were partially oxidized and exhibited residual corrosion features; c. Py2-bearing silica matrix cross-cut by later stage quartz veins; d. Ccp2 replacing Py3 in quartz vein, chalcopyrite was partially oxidized to covellite; e. Ccp2 replacing Py3 in a quartz vein, the chalcopyrite has infilled the porosity between the quartz crystals; and f. Ccp1 in altered basalt. All the photos were captured under reflected light. Ccp: chalcopyrite, Py: pyrite, Qtz: quartz, Cv: covellite, Lm: limonite, and the mineral abbreviations were according to Whitney and Evans (2010).

Table 1. Trace element composition of the pyrite from ELHF-2 (10^{-6})

Element	Reference value	Error/%	Py1(5)				Py2(15)				Py3(10)			
			Min	Max	Mean	SD	Min	Max	Mean	SD	Min	Max	Mean	SD
V	63±10	2.4	20.9	98.8	57.5	35.4	4.2	119.2	43.4	37.7	0.1	7.0	1.8	2.6
Mn	280±80	7.8	36.5	332.8	141.8	114.1	13.7	310.4	119.0	87.3	2.2	25.1	9.2	10.7
Co	60±10	6.0	113.9	834.8	492.6	303.8	252.7	1 398.2	687.6	378.0	4.0	459.1	192.9	141.6
Ni	97±15	4.4	82.4	167.5	129.2	39.1	21.2	586.7	200.7	153.6	29.6	1 245.3	450.4	434.6
Cu	134 000±500	2.0	30.5	73.3	46.6	17.0	22.9	1 759.7	234.9	473.1	446.3	6 541.7	2 985.0	2 032.4
Zn	210 000±5 000	1.4	6.9	73.4	24.4	27.7	1.9	106.3	21.3	25.9	2.7	468.4	70.7	150.3
Ga	64±11	3.5	0.2	1.8	0.8	0.6	0.0	1.5	0.5	0.4	0.1	0.6	0.2	0.2
Ge	–	–	0.7	1.3	1.0	0.3	0.5	1.4	1.0	0.3	0.6	1.4	0.9	0.3
As	65±3	9.6	8.3	137.0	77.6	56.9	19.1	862.2	180.5	244.7	6.5	403.5	104.3	131.4
Se	51±4	2.8	9.3	38.9	22.4	12.6	9.2	97.5	28.2	24.7	3.3	11.4	7.5	3.0
Mo	59±9	0.8	0.2	2.3	1.3	1.0	0.1	0.4	0.2	0.1	0.2	78.0	9.1	24.3
Ag	55±5	5.2	1.0	8.2	4.6	5.1	0.6	11.8	3.5	3.6	1.3	18.8	6.1	5.0
In	50	5.7	–	–	–	–	0.0	0.5	0.1	0.2	0.4	55.2	11.6	17.4
Sn	59±6	2.0	0.6	1.2	0.9	0.3	0.3	1.9	0.6	0.4	0.3	5.8	2.2	1.9
Sb	60±9	3.0	0.3	0.9	0.5	0.3	0.3	0.9	0.5	0.2	0.2	5.9	1.5	1.9
Te	15	9.3	4.5	15.7	10.5	5.1	1.7	13.0	5.9	3.7	1.7	8.1	5.3	3.0
Ba	14±5	15.5	0.8	13.2	4.2	5.3	0.4	6.4	1.8	2.1	–	–	–	–
Au	–	–	0.1	0.6	0.4	0.4	0.1	1.6	0.4	0.5	0.1	1.5	0.6	0.4
Tl	50	0.0	–	–	–	–	0.0	0.1	0.1	0.1	0.1	0.9	0.4	0.4
Pb	68±7	3.0	6.5	176.8	73.1	62.9	15.4	454.9	127.2	115.4	1.5	122.4	38.7	43.5
Bi	–	–	0.3	11.5	7.3	4.3	0.3	15.6	5.3	4.3	0.1	30.7	10.4	8.9
U	–	–	0.2	0.6	0.3	0.2	0.2	3.0	0.7	0.8	–	–	–	–

Note: The numbers in the brackets are the analyzing point numbers. Reference values of pyrite standard were cited from Danyushevsky et al. (2011). Error was calculated by comparing the reference values and the measured values of MASS-3 (N=3). – represents no data.

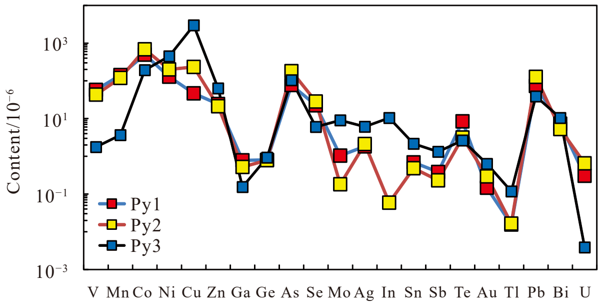

Fig. 3. Trace element contents of the pyrite from ELHF-2. Py1 and Py2 exhibit comparable compositions, whereas the trace element composition of Py3 is significantly different.

hedral, which were formed during relatively slower processes compared with anhedral pyrite, this allowed for the substitution of trace elements in the crystal lattice (Keith et al., 2016a). Therefore, this study assumed that most of the trace elements would be present in the pyrite crystal lattices as a result of Fe or S substitution, except for the V, Mn, and Cu, which would occur in the form of micro-inclusions. This was consistent with the Py1 and Py2 that had high Mn content and exhibited spikes on LA-ICP-MS time-resolved depth profiles (Fig. 4a), indicating that Mn occurred in the form of Mn-bearing mineral inclusions that were probably Mn oxides and hydroxides. The V profile was comparable with the Mn profile (Fig. 4a), which is probably the result of the absorption of V into the Mn oxide and hydroxides.

Co and Ni can substitute for Fe in the pyrite crystal lattice. However, in ELHF-2, the pyrite exhibited varied Co and Ni contents, and the LA-ICP-MS time-resolved depth profiles of Co and Ni exhibited several spikes (Figs 4a and b), indicating that they also occurred in sulfide-bearing inclusions. Py1 and Py2 showed relatively low Cu contents (average 46.6×10^{-6} and 234.9×10^{-6}, respectively) and Zn contents (24.4×10^{-6} and 21.3×10^{-6}, respectively) with generally flat (Cu) and even obscure profiles (Zn) (Fig. 4a), indicating that they mainly occurred in the crystal lattice. However, because homogeneously distributed nano-inclusions also produce flat concentration patterns, the LA-ICP-MS was not capable of distinguishing them from lattice-bound elements (Keith et al., 2016a). The solubility of Cu in pyrite is generally limited to $1\,000\times10^{-6}$–$2\,000\times10^{-6}$ under natural conditions, and the solid solution is very unstable (Reich et al., 2013). The highest Cu content in Py3 was $>6\,000\times10^{-6}$, and the LA-ICP-MS time-resolved depth profiles showed apparent spike features (Fig. 4b), indicating Cu-bearing mineral inclusions in the pyrite.

Previous studies have illustrated that arsenic can be used to discriminate trace element distribution in pyrite: either incorporated as lattice-bound substitutions or as micro- or nano-particle inclusions (Keith et al., 2016a; Martin et al., 2019). The dominant chemical form and the saturation state of Au in pyrite can be determined by a log (Au)–log (As) plot: above this limit, it is present as Au^0, whereas below this limit, it is present as Au^{+1} (Reich et al., 2005). Keith et al. (2016a), Zhang (2019) further found similar association of Au, Ag, Se, and Pb with As. In ELHF-2 samples, the Au, Ag, Se, and Pb were mainly distributed in the lattice-bound substitution zone (Fig. 5), indicating that they were mainly hosted within the pyrite structure. However, the LA-ICP-MS time-resolved depth profiles of Ag exhibited spikes features (Fig. 4b), indicating that Ag-bearing mineral inclusions were also present.

6.2 *Evolution of the mineralization environment*

In ELHF-2, differences in the trace element compositions of the pyrite generations were observed. Py1 and Py2 showed high V, Mn, and U contents, whereas Py3 contained high Cu, In, Ag, Sn, Sb, Au, and Mo contents. Previous studies have indicated that the partitioning of trace elements between the fluid phase and the corresponding pyrite is controlled by not only the bulk mineralogy but also physicochemical conditions, including temperature, pH, redox conditions, salinity, and ligand availability (Butler and Nesbitt, 1999; Keith et al., 2016a). Because of hydrothermal circulation through young oceanic crust, V and U are removed from the infiltrated seawater, causing hydrothermal fluid venting at the seafloor and the precipitation of sulfides depleted in V and U (Butler and Nesbitt, 1999; Mills et al., 1994). In the outer parts of chalcopyrite black smoker chimneys and later stage pyrite in the Rainbow vent field, the enrichment of U and V have been attributed to the interaction of seawater with the sulfide surfaces (Butler and Nesbitt, 1999; Maslennikov et al., 2009). Thus, the high V and U contents of Py1 and Py2 indicate relatively open conditions and high contents of seawater were involved in the mineralization process. This is also consistent with the higher Mn contents in Py1 and Py2 compared with Py3. Pyrite formed from high-temperature reduced fluids is characterized by low Mn contents, caused by high Mn solubility and, thus, little Mn precipitation (Maslennikov et al., 2009). This suggests that Py3 formed under more reduced conditions with a lower volume of seawater involvement, which is consistent with Py3 occurring in veinlets, whereas Py1 and Py2 occurred in disseminated forms in the altered wall rocks.

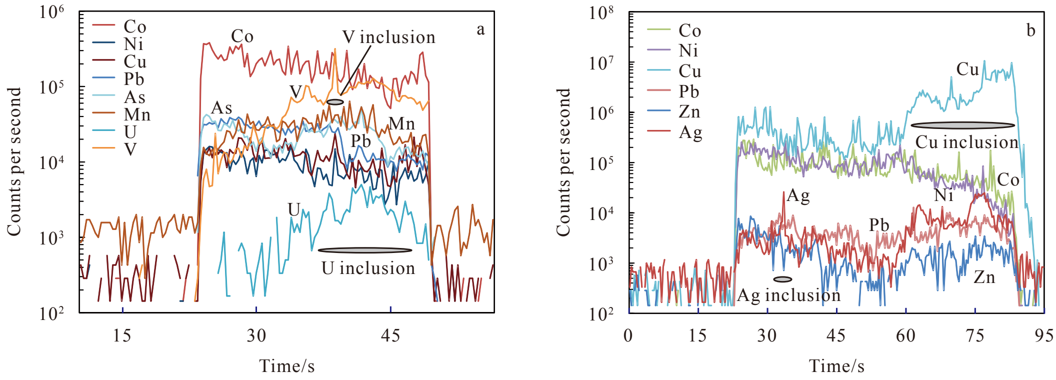

Fig. 4. Representative time-resolved laser ablation inductively coupled plasma mass spectrometry depth profiles of selected elements in Py1 (a) and Py3 (b) from ELHF-2.

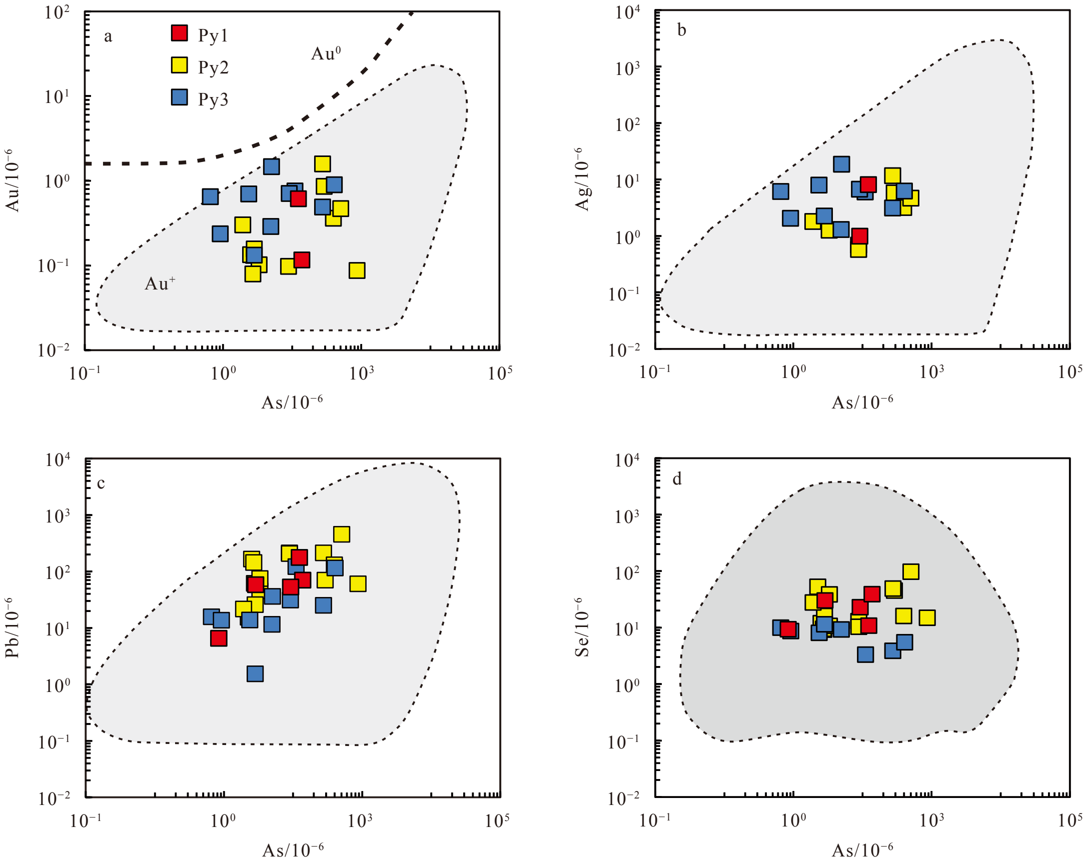

Fig. 5. Variations in Au (a), Ag (b), Pb (c), and Se (d) vs. As in pyrite from ELHF-2. The gray dashed lines define a wedge-shaped zone indicating where the Au, Ag, Pb, and Se in the pyrite crystal lattice plot within this zone (Keith et al., 2016a; Zhang, 2019).

High contents of Co and Se in pyrite are typical of high-temperature Cu-rich ores in volcanic-hosted massive sulfide deposits (Wang et al., 2017). The pyrite in the study area exhibited high Co and Ni contents (Fig. 6). These values are comparable with pyrite from a deep part of the Deep Sea Drilling Project Hole 504B and the stockwork mineralization of the volcanic massive sulfide deposit at Skouriotissa, Cyprus (Keith et al., 2016b and references therein), but significantly higher than those of massive sulfides and sulfide chimneys. This means that the samples probably represent stockwork mineralization from a high-temperature and deep part of a hydrothermal system. In addition, the incorporation of Co and Ni into pyrite is a function of temperature (T) and sulfur fugacity (fS_2), whereby Co preferentially enters the pyrite crystal lattice at high temperatures, and Ni is enriched in pyrite at relatively low temperatures (Keith et al., 2016b). Increasing fS_2 is responsible for increased Ni substitution and relatively decreased Co/Ni ratios (Meng et al., 2020). Thus, the higher Co/Ni ratios observed in Py1 and Py2 compared with Py3 (Fig. 6) also probably indicates that they formed under higher temperatures and lower fS_2 than that of Py3. This conclusion is consistent with the observation that Py1 and Py2 have high Se content, but Tl content is lower than the detection limit. Because Se is enriched with sulfides at high temperatures, whereas Tl is preferentially partitioned into sulfides under low-temperature conditions (about 100–250°C) (Hannington et al., 1995). Further, Py3 had a higher Mo content than the earlier stage pyrites (Fig. 3), probably indicating decreasing temperature during ore formation. Because the solubility of Mo in high-temperature fluids decreases sharply, causing pyrite precipitated at high temperatures to contain low amounts of Mo (Metz and Trefry, 2000). This conclusion is consistent with observations in several mid-ocean-ridge HFs and ancient HFs on land (Martin et al., 2019). Therefore, it can be concluded that Py1 and Py2 formed under relatively open and high-temperature conditions with greater seawater involvement, whereas Py3 was formed under higher fS_2 conditions than the earlier stages of pyrite deposition.

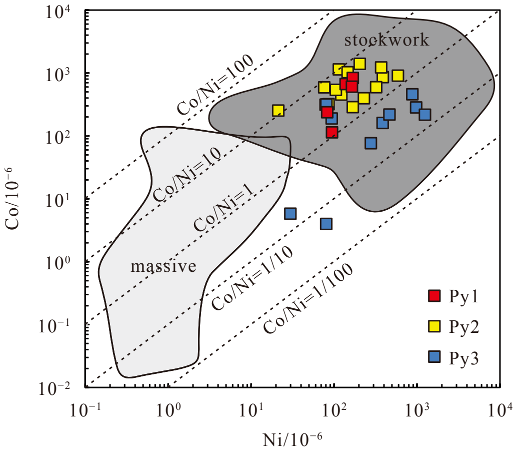

Fig. 6. Variations in Co vs. Ni content in pyrite from stockwork and massive sulfides. The dark grey area representing pyrite from DSDP Hole 504B and stockwork mineralization of Skouriotissa, while the light-grey domain representing massive sulfide and sulfide chimneys (according to Keith et al., 2016b).

6.3 *The origin of the ore-forming elements*

Pyrite from ELHF-2 was enriched in Co, Ni, Mn, Cu, Zn, As, and Pb. Previous studies have pointed out that the composition of the host rock is a critical factor for differences in trace element enrichment in seafloor hydrothermal systems (Wohlgemuth-Ueberwasser et al., 2015). It has been observed that ultramafic-related hydrothermal systems are characterized by higher Au contents in sulfides (>3×10^{-6} average Au) than mafic-related hydrothermal systems (German et al., 2016). As for pyrite, Keith et al. (2016a) found that pyrite in ultramafic-related HFs exhibit apparent Au enrichment and As depletion compared with that of mafic-related hydrothermal systems, and proposed that serpentinization plays an important role in Au enrichment. Therefore, the combined As contents and Au/As and Ag/As ratios of pyrite can be used to discriminate between mafic-related and ultramafic-related HFs (Keith et al., 2016a). In addition, sulfide minerals in several ultramafic-related HFs have been observed to have high Ni content, probably resulted from the interaction of hydrothermal fluids with an ultramafic basement containing higher Ni concentrations than mafic rocks (Marques et al., 2007; Wang et al., 2017). Melekestseva et al. (2013) concluded that Ni/Co ratios <1 in seafloor deposits indicate a dominant contribution of metals from a mafic rather than an ultramafic source.

In ELHF-2 samples, the pyrite was distributed in both disseminated (Py1 and Py2) and veinlet (Py3) forms in the altered basalt (Fig. 2), which strongly suggests that basalt played an important role in the mineralization. However, the pyrite exhibited high Ni contents, high Au/As and Ni/As ratios that were comparable with the Logatchev field but significantly different from those of the hybrid Kairei and Longqi-1 fields, the mafic-related Meso zone and Wocan field, and the HFs at the 5°S East Pacific Rise (Fig. 7a). This strongly indicates that this field is ultramafic related. In addition, Py3 showed even higher Ni/As and Au/As ratios than those of Py1 and Py2, indicating that the ore-forming elements derived from ultramafic rock increased during the ore-forming process. This is also consistent with Py3 exhibited higher Ni content and lower Co/Ni ratios than Py1 and Py2 (Figs 6 and 7b), and also showed consistency with As content and Au/As and Ag/As ratios of the Py3 plotted in areas closer to the ultramafic-related Logatchev field than those of Py1 and Py2 (Figs 7a and b). Therefore, this study suggest that the ore-forming elements of ELHF-2 were derived from ultramafic rocks.

6.4 *Indications of ore genesis*

ELHF-2 developed on the surface of the Dragon Horn OCC and the pyrite geochemistry suggests that the ore-forming elements are of ultramafic origin, indicating that it belongs to the ultramafic-related HFs. On ultraslow-spreading ridges, HFs controlled by OCCs comprise about half the HFs (German et al., 2016), including the Petersburg, Saldanha, Rainbow, Logatchev, Lost City, Semyenov, Irinovskoe, Lilliput, Ashadze, Nibelungen, Von Damm, and Tianzuo fields (Beaulieu et al., 2015 and references therein). These fields are exclusively located on ridge flanks that are up to 16 km from the ridge axis. The proposed heat source for some of these systems (e.g., the Lost City and Saldanha fields) are exothermic serpentinization reactions between seawa-

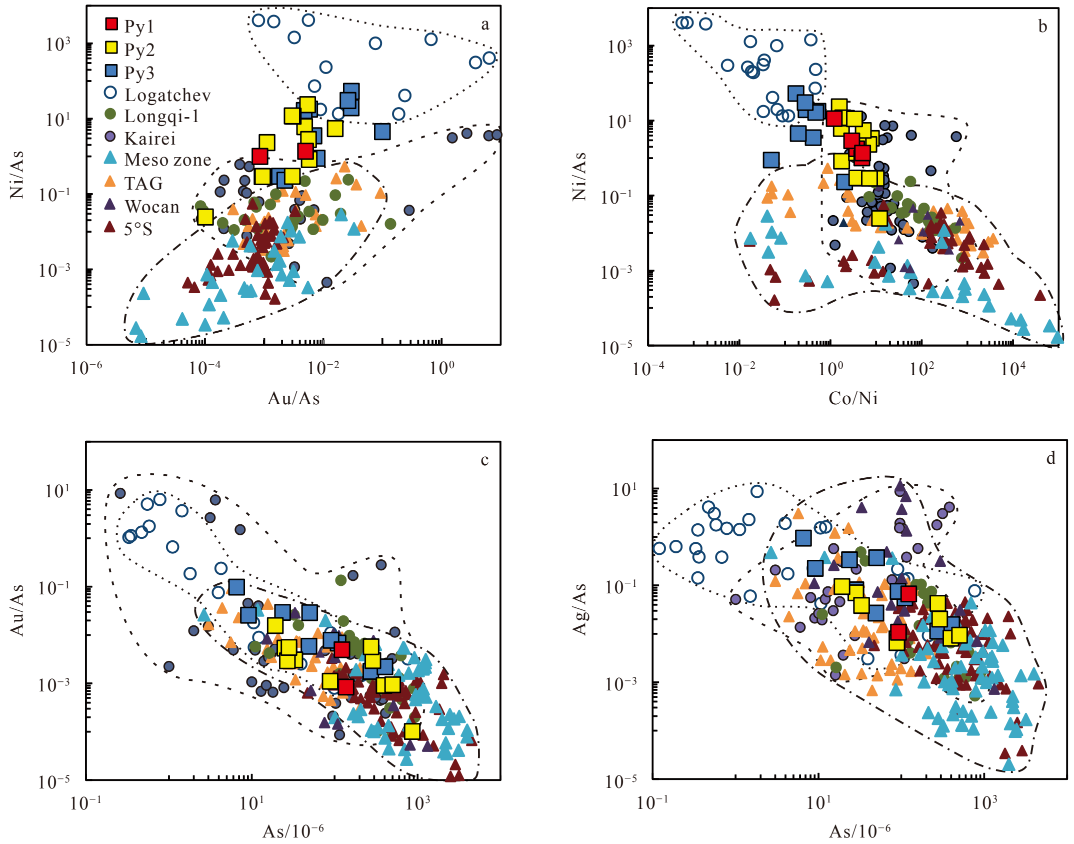

Fig. 7. Variations in Au/As vs. Ni/As (a), Co/Ni vs. Ni/As (b), As vs. Au/As (c), and As vs. Ag/As (d) in pyrite from ultramafic- and mafic-related hydrothermal systems at MORs. The dot line, short dash line and dash-dot line indicates ultramafic, hybrid and mafic area, respectively. Database: Longqi-1 (Yuan et al., 2018); Kairei (Keith et al., 2016a; Wang et al., 2018); Logatchev, TAG, Meso zone, and 5°S East Pacific Rise (Keith et al., 2016a); and Wocan (Wang et al., 2017).

ter and underlying peridotite (Dias and Barriga, 2006; Kelley et al., 2001), whereas high-temperature hydrothermal systems, such as the Rainbow and Logatchev fields, seem to depend on an additional magmatic heat source (Andersen et al., 2015; Marques et al., 2007).

ELHF-2, located about 12 km away from the ridge axis, is among the fields that are furthest from the ridge axis. Hydrothermal systems cannot directly mine heat from a ridge axis at such a large distance (Fontaine et al., 2017; Lowell et al., 2007), which suggests that it is probably driven by exothermic serpentinization reactions. However, the pyrite geochemistry suggests high formation temperatures of this field. The appearance of chalcopyrite also indicates that the temperature of the hydrothermal mineralization was greater than 250°C, and the appearance of euhedral quartz crystals in a sulfide-bearing quartz vein also indicates a high-temperature ore-forming fluid, excluding the possibility that the associated hydrothermal circulation of this field belongs to low-temperature diffuse flow. Heat balance models have suggested that the serpentinization of peridotites is most likely to result in hydrothermal venting at temperatures ranging from a few degrees to a few tens of degrees (Lowell and Rona, 2002). Allen and Seyfried (2004) further suggested that exothermic serpentinization reactions are ineffective for creating hydrothermal circulation, especially at relatively low and high temperatures due to kinetic constraints. Therefore, this study propose that ELHF-2 was formed by exothermic serpentinization reactions with an additional magmatic heat that probably supplied by a sill or dike.

7 Conclusions

This study investigated pyrite and its chemical compositions from ELHF-2 at Southwest Indian Ridge. Based upon the formation sequence of sulfide and gangue minerals, three stages of pyrite mineralization could be classified: Py1 and Py2, distributed in the altered basalt debris and the silica altered matrix, respectively, exhibiting V, Mn, U, and Se enrichment features; while, Py3, mainly occurs in quartz veins, was intergrown with chalcopyrite, with high Cu, In, Ag, Sb, and Au contents. Combing with previous studies, the data show that the trace elements, such as Au, Se, and Pb, mainly substitute Fe in the pyrite crystal lattice; in contrast, Cu, Zn, Co, Ni, and Ag are likely present both as Fe substitution and as micro- to nanoparticle-sized mineral inclusions. In addition, V, Mn, and U are probably in the form of oxide inclusions. Furthermore, pyrite in the studied hydrothermal system was formed at high-temperature conditions, but fluid temperature was decreased from early to late stage during the ore-forming process. Comparing with Py3, Py1 and Py2 were formed under higher water/rock ratio and higher temperature conditions and involved greater volumes of seawater during mineralization. In conclusion, the ELHF-2 field is probably ultramafic related and formed by exothermic serpentinization reactions with an additional magmatic heat source, and chemical compositions of pyrite could provide detailed information on sulfide mineralization in hydrothermal systems.

Acknowledgements

We thank the captains and crews of the DY125-40 cruise on R/V *Xiangyanghong 10*, who contributed to the success of this project.

References

Allen D E, Seyfried W E Jr. 2004. Serpentinization and heat generation: constraints from Lost City and Rainbow hydrothermal systems. Geochimica et Cosmochimica Acta, 68(6): 1347–1354, doi: 10.1016/j.gca.2003.09.003

Andersen C, Rüpke L, Hasenclever J, et al. 2015. Fault geometry and permeability contrast control vent temperatures at the Logatchev 1 hydrothermal field, Mid-Atlantic Ridge. Geology, 43(1): 51–54, doi: 10.1130/G36113.1

Beaulieu S E, Baker E T, German C R. 2015. Where are the undiscovered hydrothermal vents on oceanic spreading ridges?. Deep-Sea Research Part Ⅱ: Topical Studies in Oceanography, 121: 202–212, doi: 10.1016/j.dsr2.2015.05.001

Bemis K, Lowell R P, Farough A. 2012. Diffuse flow on and around hydrothermal vents at mid-ocean ridges. Oceanography, 25(1): 182–191, doi: 10.5670/oceanog.2012.16

Butler I B, Nesbitt R W. 1999. Trace element distributions in the chalcopyrite wall of a black smoker chimney: insights from laser ablation inductively coupled plasma mass spectrometry (LA–ICP–MS). Earth and Planetary Science Letters, 167(3–4): 335–345, doi: 10.1016/S0012-821X(99)00038-2

Chen Jie, Tao Chunhui, Liang Jin, et al. 2018. Newly discovered hydrothermal fields along the ultraslow-spreading Southwest Indian Ridge around 63°E. Acta Oceanologica Sinica, 37(11): 61–67, doi: 10.1007/s13131-018-1333-y

Corliss J B, Dymond J, Gordon L I, et al. 1979. Submarine thermal springs on the Galapagos Rift. Science, 203(4385): 1073–1083, doi: 10.1126/science.203.4385.1073

Danyushevsky L, Robinson P, Gilbert S, et al. 2011. Routine quantitative multi-element analysis of sulphide minerals by laser ablation ICP-MS: Standard development and consideration of matrix effects. Geochemistry: Exploration, Environment, Analysis, 11(1): 51–60, doi: 10.1144/1467-7873/09-244

Dias Á S, Barriga F J A S. 2006. Mineralogy and geochemistry of hydrothermal sediments from the serpentinite-hosted Saldanha hydrothermal field (36°34′N; 33°26′W) at MAR. Marine Geology, 225(1–4): 157–175, doi: 10.1016/j.margeo.2005.07.013

Dick H J B, Lin Jian, Schouten H. 2003. An ultraslow-spreading class of ocean ridge. Nature, 426(6965): 405–412, doi: 10.1038/nature02128

Fontaine F J, Rabinowicz M, Cannat M. 2017. Can high-temperature, high-heat flux hydrothermal vent fields be explained by thermal convection in the lower crust along fast-spreading Mid-Ocean Ridges?. Geochemistry, Geophysics, Geosystems, 18(5): 1907–1925, doi: 10.1002/2016GC006737

Fouquet Y, Cambon P, Etoubleau J, et al. 2010. Geodiversity of hydrothermal processes along the Mid-Atlantic Ridge–Ultramafic-hosted mineralization: A new type of oceanic Cu-Zn-Co-Au volcanogenic massive sulfide deposit. In: Rona P A, Devey C W, Dyment J, et al., eds. Diversity of Hydrothermal Systems on Slow Spreading Ocean Ridges. Washington DC: American Geophysical Union, 188, 321–367

Georgen J E, Lin Jian, Dick H J B. 2001. Evidence from gravity anomalies for interactions of the Marion and Bouvet hotspots with the Southwest Indian Ridge: Effects of transform offsets. Earth and Planetary Science Letters, 187(3–4): 283–300, doi: 10.1016/S0012-821X(01)00293-X

German C R, Petersen S, Hannington M D. 2016. ydrothermal exploration of mid-ocean ridges: Where might the largest sulfide deposits be forming?. Chemical Geology, 420: 114–126, doi: 10.1016/j.chemgeo.2015.11.006

Hannington M D, De Ronde C D, Petersen S. 2005. Sea-floor tectonics and submarine hydrothermal systems. In: Hedenquist J W, Thompson J F H, Goldfarb R J, et al., eds. One Hundredth Anniversary Volume. McLean VA: Society of Economic Geologists, 100: 111–141

Hannington M D, Tivey M K, Larocque A C, et al. 1995. The occurrence of gold in sulfide deposits of the TAG hydrothermal field, Mid-Atlantic Ridge. The Canadian Mineralogist, 33(6): 1285–1310

Haymon R M. 1983. Growth history of hydrothermal black smoker chimneys. Nature, 301(5902): 695–698, doi: 10.1038/301695a0

Keith M, Häckel F, Haase K M, et al. 2016a. Trace element systematics of pyrite from submarine hydrothermal vents. Ore Geology

Reviews, 72: 728–745, doi: 10.1016/j.oregeorev.2015.07.012

Keith M, Haase K M, Klemd R, et al. 2016b. Systematic variations of trace element and sulfur isotope compositions in pyrite with stratigraphic depth in the Skouriotissa volcanic-hosted massive sulfide deposit, Troodos ophiolite, Cyprus. Chemical Geology, 423: 7–18, doi: 10.1016/j.chemgeo.2015.12.012

Kelley D S, Karson J A, Blackman D K, et al. 2001. An off-axis hydrothermal vent field near the Mid-Atlantic Ridge at 30°N. Nature, 412(6843): 145–149, doi: 10.1038/35084000

Li Jiabiao, Jian Hanchao, Chen J Y, et al. 2015. Seismic observation of an extremely magmatic accretion at the ultraslow spreading Southwest Indian Ridge. Geophysical Research Letters, 42(8): 2656–2663, doi: 10.1002/2014GL062521

Liao Shili, Tao Chunhui, Li Huaming, et al. 2018. Bulk geochemistry, sulfur isotope characteristics of the Yuhuang-1 hydrothermal field on the ultraslow-spreading Southwest Indian Ridge. Ore Geology Reviews, 96: 13–27, doi: 10.1016/j.oregeorev.2018.04.007

Lowell R P, Gosnell S, Yang Yang. 2007. Numerical simulations of single-pass hydrothermal convection at mid-ocean ridges: Effects of the extrusive layer and temperature-dependent permeability. Geochemistry, Geophysics, Geosystems, 8(10): Q10011, doi: 10.1029/2007GC001653

Lowell R P, Rona P A. 2002. Seafloor hydrothermal systems driven by the serpentinization of peridotite. Geophysical Research Letters, 29(11): 26–1

Marques A F A, Barriga F J A S, Scott S D. 2007. Sulfide mineralization in an ultramafic-rock hosted seafloor hydrothermal system: From serpentinization to the formation of Cu–Zn–(Co)-rich massive sulfides. Marine Geology, 245(1–4): 20–39, doi: 10.1016/j.margeo.2007.05.007

Marques A F A, Scott S D, Guillong M. 2011. Magmatic degassing of ore-metals at the Menez Gwen: Input from the Azores plume into an active Mid-Atlantic Ridge seafloor hydrothermal system. Earth and Planetary Science Letters, 310(1–2): 145–160, doi: 10.1016/j.epsl.2011.07.021

Martin A J, Keith M, McDonald I, et al. 2019. Trace element systematics and ore-forming processes in mafic VMS deposits: Evidence from the Troodos ophiolite, Cyprus. Ore Geology Reviews, 106: 205–225, doi: 10.1016/j.oregeorev.2019.01.024

Maslennikov V V, Maslennikova S P, Large R R, et al. 2009. Study of trace element zonation in vent chimneys from the Silurian Yaman-Kasy volcanic-hosted massive sulfide deposit (Southern Urals, Russia) using laser ablation-inductively coupled plasma mass spectrometry (LA-ICPMS). Economic Geology, 104(8): 1111–1141, doi: 10.2113/gsecongeo.104.8.1111

Melekestseva I Y, Zaykov V V, Nimis P, et al. 2013. Cu–(Ni–Co–Au)-bearing massive sulfide deposits associated with mafic–ultramafic rocks of the Main Urals Fault, South Urals: Geological structures, ore textural and mineralogical features, comparison with modern analogs. Ore Geology Reviews, 52(4): 18–36

Meng Xingwei, Li Xiaohu, Chu Fengyou, et al. 2020. Trace element and sulfur isotope compositions for pyrite across the mineralization zones of a sulfide chimney from the East Pacific Rise (1–2°S). Ore Geology Reviews, 116: 103209, doi: 10.1016/j.oregeorev.2019.103209

Metz S, Trefry J H. 2000. Chemical and mineralogical influences on concentrations of trace metals in hydrothermal fluids. Geochimica et Cosmochimica Acta, 64(13): 2267–2279, doi: 10.1016/S0016-7037(00)00354-9

Mills R A, Thomson J, Elderfield H, et al. 1994. Uranium enrichment in metalliferous sediments from the Mid-Atlantic Ridge. Earth and Planetary Science Letters, 124(1–4): 35–47, doi: 10.1016/0012-821X(94)00083-2

Murton B J, Lehrmann B, Dutrieux A M, et al. 2019. Geological fate of seafloor massive sulphides at the tag hydrothermal field (mid-Atlantic ridge). Ore Geology Reviews, 107: 903–925, doi: 10.1016/j.oregeorev.2019.03.005

Reich M, Deditius A, Chryssoulis S, et al. 2013. Pyrite as a record of hydrothermal fluid evolution in a porphyry copper system: A SIMS/EMPA trace element study. Geochimica et Cosmochimica Acta, 104: 42–62, doi: 10.1016/j.gca.2012.11.006

Reich M, Kesler S E, Utsunomiya S, et al. 2005. Solubility of gold in Arsenian pyrite. Geochimica et Cosmochimica Acta, 69(11): 2781–2796, doi: 10.1016/j.gca.2005.01.011

Sauter D, Cannat M, Meyzen C, et al. 2009. Propagation of a melting anomaly along the ultraslow Southwest Indian Ridge between 46°E and 52°20′E: Interaction with the Crozet hotspot?. Geophysical Journal International, 179(2): 687–699, doi: 10.1111/j.1365-246X.2009.04308.x

Tao Chunhui, Li Huaiming, Huang Wei, et al. 2011. Mineralogical and geochemical features of sulfide chimneys from the 49°39′ E hydrothermal field on the Southwest Indian Ridge and their geological inferences. Chinese Science Bulletin, 56(26): 2828–2838, doi: 10.1007/s11434-011-4619-4

Tao Chunhui, Li Huaming, Jin Xiaobing, et al. 2014. Seafloor hydrothermal activity and polymetallic sulfide exploration on the Southwest Indian Ridge. Chinese Science Bulletin, 59(19): 2266–2276, doi: 10.1007/s11434-014-0182-0

Tao Chunhui, Lin Jian, Guo Shiqin, et al. 2012. First active hydrothermal vents on an ultraslow-spreading center: Southwest Indian Ridge. Geology, 40(1): 47–50, doi: 10.1130/G32389.1

Tao Chunhui, Seyfried W E Jr, Lowell R P, et al. 2020. Deep high-temperature hydrothermal circulation in a detachment faulting system on the ultra-slow spreading Ridge. Nature Communications, 11: 1300, doi: 10.1038/s41467-020-15062-w

Wang Yejian, Han Xiqiu, Petersen S, et al. 2017. Mineralogy and trace element geochemistry of sulfide minerals from the Wocan Hydrothermal Field on the slow-spreading Carlsberg Ridge, Indian Ocean. Ore Geology Reviews, 84: 1–19, doi: 10.1016/j.oregeorev.2016.12.020

Wang Yejian, Han Xiqiu, Petersen S, et al. 2018. Trace metal distribution in sulfide minerals from ultramafic-hosted hydrothermal systems: examples from the Kairei vent field, central Indian ridge. Minerals, 8(11): 526, doi: 10.3390/min8110526

Whitney D L, Evans B W. 2010. Abbreviations for names of rock-forming minerals. American Mineralogist, 95(1): 185–187, doi: 10.2138/am.2010.3371

Wohlgemuth-Ueberwasser C C, Viljoen F, Petersen S, et al. 2015. Distribution and solubility limits of trace elements in hydrothermal black smoker sulfides: An in-situ LA-ICP-MS study. Geochimica et Cosmochimica Acta, 159: 16–41, doi: 10.1016/j.gca.2015.03.020

Yang Weifang, Tao Chunhui, Li Huaming, et al. 2016. ^{230}Th/^{238}U dating of hydrothermal sulfides from Duanqiao hydrothermal field, Southwest Indian Ridge. Marine Geophysical Research, 38(1): 71–83

Ye Jun, Shi Xuefa, Yang Yaomin, et al. 2012. The occurrence of gold in hydrothermal sulfide at Southwest Indian Ridge 49. 6°E. Acta Oceanologica Sinica, 31(6): 72–82

Yuan Bo, Yu Hongjun, Yang Yaomin, et al. 2018. Zone refinement related to the mineralization process as evidenced by mineralogy and element geochemistry in a chimney fragment from the Southwest Indian Ridge at 49. 6°E. Chemical Geology, 482: 46–60

Zhang Bosong. 2019. Study of mineralization at the Longqi and Duanqiao hydrothermal fields, Southwest Indian Ridge (in Chinese) [dissertation]. Beijing: China University of Geosciences (Beijing)

Zhang Jing, Deng Jun, Chen Huayong, et al. 2014. LA-ICP-MS trace element analysis of pyrite from the Chang'an gold deposit, Sanjiang region, China: Implication for ore-forming process. Gondwana Research, 26(2): 557–575, doi: 10.1016/j.gr.2013.11.003

Zhao Haixiang, Frimmel H E, Jiang Shaoyong, et al. 2011. LA-ICP-MS trace element analysis of pyrite from the Xiaoqinling gold district, China: Implications for ore genesis. Ore Geology Reviews, 43(1): 142–153, doi: 10.1016/j.oregeorev.2011.07.006